Environmental Science and Ecotechnology 4 (2020) 100062

Contents lists available at ScienceDirect

Environmental Science and Ecotechnology

journal homepage: www.journals.elsevier.com/environmental-science-and-ecotechnology/

Original Research

Monitoring stratification of anode biofilms in bioelectrochemical laminar flow reactors using flow cytometry

Yuting Guo, Luis F.M. Rosa, Susann Müller, Falk Harnisch*

Department of Environmental Microbiology, Helmholtz-Centre for Environmental Research – UFZ, Permoserstrasse 15, 04318, Leipzig, Germany

ARTICLE INFO

Article history:
Received 22 July 2020
Received in revised form
25 September 2020
Accepted 26 September 2020

Keywords:
Microbial electrochemical technology
Flow cytometry
Laminar flow
Microbial community
Electroactive microorganisms

ABSTRACT

A laminar flow bioelectrochemical systems (BES) was designed and benchmarked using microbial anodes dominated with *Geobacter* spp. The reactor architecture was based on modeled flow fields, the resulting structure was 3D printed and used for BES manufacturing. Stratification of the substrate availability within the reactor channels led to heterogeneous biomass distribution, with the maximum biomass found mainly in the initial/middle channels. The anode performance was assessed for different hydraulic retention times while coulombic efficiencies of up to 100% (including also hydrogen recycling from the cathode) and current densities of up to 75 μA cm^{-2} at an anode surface to volume ratio of 1770 cm^2 L^{-1} after 35 days were achieved. This low current density can be clearly attributed to the heterogeneous distributions of biomass and the stratification of the microbial community structure. Further, it was shown that time and space resolved analysis of the reactor microbiomes per channel is feasible using flow cytometry.

1. Introduction

Microbial electrochemical technologies (MET) possess promising potential in environmental and industrial biotechnology [1]. Among the envisaged application are MET for waste water (WW) treatment and valorization [2,3]. In primary MET microbial anodes allow the oxidation of highly diverse substrates that can serve as carbon sources and electron donors. These substrates are oxidized by electrochemically active microorganisms (EAM) and the electrons are transferred to the anode via extracellular electron transfer [4,5] (EET). Thus, the metabolism of microbiomes inhering EAM allows converting waste streams into electric energy. A number of different reactor types for primary MET, also known as bioelectrochemical systems (BES), do exist [6]. Yet, BES for WW treatment are still far from full-scale application. Among others, this can be assigned to the lack of standards and comparable reactor systems and the hence insufficient benchmarking of components like membranes or electrode materials and architecture [7,8]. Thus, it is not feasible to fully compare the performance indicators between different studies, even for the same type of process, which also hampers a knowledge-driven development of components and process engineering [9]. The core element of all BES treating WW is the microbial anode. At the anode, the interplay of electrode material and architecture and microbial community inhering EAM, is the key for successful WW treatment and electron harvest. This interplay was shown to be highly complex and dependent on the relationship between abiotic parameters like substrate composition and concentration, reactor and electrode design as well as the microbiome [10–12]. This complex interplay needs to be revealed in order to allow a future knowledge-driven engineering of BES [13,14].

Very few BES allow performing analysis on the reactor microbiome, including the biofilm community within the reactors in time or space [12,15]. Generally, in the utmost majority of studies, the BES performance is assessed mainly on the physical-chemical level, e.g., current or gas production, pH, temperature and chemical oxygen demand (COD) removal. The microbial activity, the dynamic biofilm formation and temporal as well as local composition have been rather a subject of selective characterization [16,17] than active monitoring. In situ imaging provides certainly a promising option, but is restricted to non-invasive technologies such as confocal Raman microscopy [18] and optical coherence tomography [19] or only provides limited information on the identification of microorganisms. However, this identification is of highest importance for

* Corresponding author.
E-mail address: falk.harnisch@ufz.de (F. Harnisch).

https://doi.org/10.1016/j.ese.2020.100062

long-term operation, especially for chemically complex substrates and when the distribution of substrate is not equal within a reactor system. This is the case for most scaled-up BES, where the necessary mixing power for keeping the bulk substrates homogeneous in the reactor cannot be implemented due to the high sheer stress on the electroactive biofilms [20–22].

Therefore we introduce here an electrochemical laminar flow reactor inspired by reactors used for abiotic electrochemistry [23] for cultivating biofilm electrodes that is cheap and can be easily tailored to allow the spatial analysis of microbial communities. The laminar flow reactor was created using finite element modelling and subsequent 3D printing. It was inoculated with enriched electrochemically active biofilm and operated using acetate as the sole carbon source, as this approach is very often used for studies on, for instance, developing electrode materials or reactors [24–26]. Variable flow rates were applied both to set a nutrient gradient in the system, and to ascertain the acetate removal capacity and current production efficiency of the biofilm. The microbial community was monitored dynamically by flow cytometry. It has been proved to be a fast, reliable and comparable tool and to be of a similar resolution as a 16S rRNA gene analysis [27–31]. The application of flow cytometry for characterization, quantification and evaluation of microbiomes in BES has been introduced and is used increasingly [32–35]. Besides its use in bioreactors, this technology has also been applied to large-scale wastewater treatment plants (WWTP) for long-term investigations of dynamic community assembly, to discover perturbation-associated symptoms for community control [36], or for automatic online monitoring, where the community data obtained was used as an early-warning tool to reflect/control drinking water process operation [37,38]. The here presented study aimed to analyze the stratification of the microbial communities and the interactions between the microorganism and the substrate. The study shall serve as a benchmark for follow-up studies at more complex conditions. This will allow to gain a full understanding of EAM selection and stratification when facing complex substrates and gradients thereof needing the creation of microbial food-webs.

2. Materials and methods

2.1. Reactor design and manufacturing

The reactors were designed using the CAD interface of COMSOL Multiphysics (Comsol Multiphysics GmbH, Göttingen, Germany) (SI Figure S1 A and B). The CAD geometries were exported and sliced using the program Ultimaker CURA (Ultimaker 2+, Geldermalsen, The Netherlands) for 3D printing of the flow channels, with highest quality settings and 100% infill, using 2.75 mm Ø poly-lactic-acid (PLA) filament (Innofil PLA, BASF 3D Printing Solutions BV, Emmen, The Netherlands).

Graphite plates (CP-2200®, CP Handels-GmbH Wachtberg, Germany) were cut into 200 × 135 × 2 mm pieces and were used as electrodes. To prepare the anodic and cathodic chambers, one surface of each graphite plate was first covered with epoxy resin adhesive (Cat. Nr: 886598- 62, Conrad Electronic SE, Hirschau, Germany) for air and liquid tight insulation. The opposing surface of the plate was carefully glued to one of the 3D printed flow channel assemblies, creating a continuous set of flow channels at the surface of the graphite plate with an effective geometric electrode surface area of 170 cm^2 distributed through 16 channels. Pictures with a scale for the dimension of the final built flow channel reactors can be found in SI Figure S1. A reference electrode with 5 mm diameter and 100 mm length (Ag/AgCl sat. KCl, SE11, Xylem Analytics, Meinsberg, Germany) was placed inside channel 9 (C9), using silicone for insulation. The anode potential was kept at +200 mV versus the potential of the reference electrode. Both the anode and cathode chambers were carefully assembled by sandwiching a cation exchange membrane (FKE-50, Lot-No: M21471301, FuMA-Tech, Ingbert, Germany). The membrane was glued to both sides with epoxy glue (Loctite Hysol 3430, Henkel, Düsseldorf, Germany). Each chamber possessed inlet and outlet using tygon tubing (internal diameter: 1.6 mm, wall thickness: 0.8 mm, Cat. Nr: 9205536, Th. Geyer, Renningen, Germany). For quality control after assembly, each reactor was tested to confirm no liquid communication between the anode and cathode chambers and liquid tightness before inoculation.

In order to provide a uniform potential distribution across the plates, each plate was connected using four connections, which were spaced equally along the two long sides. The assembling process and the reactor are displayed in SI Figure S2.

2.2. Experimental setup and operation

Three independent reactors were studied and terminated at different times. The reactors were operated under nearly anaerobic conditions and therefore difficult to sample microorganisms online, hence our strategy was to sacrifice the reactors for microbial sampling as detailed below. All experiments were carried out at 35 °C. Two modes of reactor operation were used: an initial 7-day batch mode followed by a 28-day continuous mode.

To prepare the inoculum, steady-state anodic biofilms were harvested from a potentiostatically controlled bioelectrochemical fed-batch reactor with a reproducible maximum current density of 600 μA cm^{-2} dominated by *Geobacter* spp. [32]. (as described elsewhere [39]). The biofilms were suspended in artificial wastewater supplemented with sodium acetate as the only carbon source (10 mM) and vitamin and trace metal solutions [40]. The optical density was adjusted to OD_{600} = 0.02 (Ultrospec 1100pro, Amersham Biosciences, Buckinghamshire, UK). This mixture served as inoculum solution and was further purged with nitrogen for 30 min before being pumped into the anode chamber of each reactor (96 mL per reactor). At this time, one inoculum sample was fixed (see below) and stored for further measurements by flow cytometry [41].

To start the 7-day batches, the anodic chambers of all three reactors were filled with inoculum solution, and the cathodic chambers were filled with the same medium free of carbon source and microorganisms. The inlet and outlet tubes were closed using airtight plugs. The reactors were controlled using a multichannel potentiostat (MPG-2, Bio-Logic SAS, Claix, France). The electrochemical parameters like potential of working electrode (that is the anode) and counter electrode (that is the cathode), current, and total charge were recorded with intervals of 10 min.

After three reactors achieved a reproducible plateau of current production within the batch cultivation, the continuous mode was started. During this time, a growth of electroactive biofilms took place where the dominance of *Geobacter* spp. can be further expected [10,32]. It has been reported that the doubling times of *Geobacter* spp. ranged from 6 h to 24 h, depending on the different applied potentials [42] or electron acceptors [43]. Therefore, in this study, an initial hydraulic retention time (HRT) of 24 h was applied, first from days 8–15. Following, the HRT was decreased from days 16–20 with HRT = 17 h, days 21–28 with HRT = 14 h, and days 29–35 with HRT = 12 h. On day 20, reactor 1 was stopped for biofilm harvest: the anode chamber was carefully separated from the cathode chamber, and the biofilm formed in each channel was carefully scratched off into an individual Eppendorf tube, and was resuspended to 2 mL of phosphate buffered saline (PBS, composition can be found in SI Table S1). The biomass production in each channel (SI Figure S3) was estimated via OD_{600} measurement after resuspension. All samples (16 biofilm samples + 1 outlet sample per

reactor) were fixed and stored at −20 °C until flow cytometric measurement. On day 28 reactor 2 and on day 35 reactor 3 were stopped for biofilm harvest using the procedure described above. For the duration of the continuous operation mode, both acetate concentration and pH of the outlet solution were measured daily. Acetate was quantified by HPLC using a HiPlex H-column 300 × 7.7 mm (Agilent Technologies, Inc. CA, USA) with a SecurityGuard Cartridge Carbo-H 4 × 3.0 mm pre-column (Phenomenex, USA) and refractive index detector (RID-10A, Shimadzu Europa GmbH, Duisburg, Germany). The chromatograms were obtained isocratically for 30 min, where the mobile phase was 0.01 N sulfuric acid and the flow rate was 0.5 mL min^{-1}. The column oven temperature was set to 50 °C. Prior to HPLC analysis the samples were centrifuged in a microcentrifuge (MiniSpin, Eppendorf AG, Wesseling-Berzdorf, Germany) for 5 min with 8000×*g* at room temperature (RT) and subsequently filtered with 0.2 μm nylon filters. The pH was measured using a portable pH meter (LAQUAtwin pH Meter, HORIBA Europe GmbH, Oberursel, Germany).

2.3. Calculations

Current densities were calculated by dividing the recorded current by the anodic geometric surface area [44]:

$$j = i/S \quad (1)$$

While j is current density [A m^{-2}], i is current [A], and S is the anodic geometric surface area for each reactor [m^2] that is 170 cm^2.

Coulombic efficiencies were determined by comparison of the total produced amount of electrons (total charge, Q_p) per the theoretical maximum number of electrons (Q_{th}) which is calculated from acetate consumption within a certain time interval [39], assuming a theoretical maximum yield of 8 mol of electrons per mole of acetate [45].

$$CE = \frac{Qp}{Qth} \times 100 \quad (2)$$

$$Qth = \frac{F \times z \times c \times V_i}{M} \quad (3)$$

While CE is coulombic efficiency, Q_p is the produced amount of electrons, Q_{th} is the theoretical amount of electrons calculated from acetate consumption, F is Faraday's constant [96485 C mol^{-1}], z is the number of electrons produced per mol of acetate ($z = 8$), c is the acetate concentration [g L^{-1}], V_i is the medium volume for a given time interval [L], and M is the molecular weight of acetate.

2.4. Flow cytometric measurement and data analysis

2.4.1. Cell fixation

The samples were centrifuged (3200×*g*, 10 min, 4 °C). Then the cell pellets were re-suspended in 4 mL of 2% paraformaldehyde (PFA) in PBS for 30 min at RT and centrifuged (as before). After removing the supernatant, the cell pellets were re-suspended in 4 mL of 70% ethanol in Milli-Q water and stored at −20 °C until staining [30]. Details of PFA and PBS compositions and Milli-Q water are given in SI Table S1.

2.4.2. Cell staining

Fixed samples were diluted into 1 mL of PBS and ultra-sonicated (ultrasonic bath, Merck Eurolab, Darmstadt, Germany, 35 kHz at RT) for 5 min before centrifugation (as before). Then the cell pellets were re-suspended in 1 mL of PBS, ultra-sonicated again for 10 min, and adjusted to $OD_{700} = 0.035$ within 1 mL PBS before centrifugation (as before). Finally, the cell pellets were re-suspended in 0.5 mL of stock A (permeabilization buffer, 20 min, at RT), centrifuged (as before), then re-suspended in 1 mL of stock B (DAPI staining solution, overnight, dark, at RT) until flow cytometric measurement [30]. The compositions of stock A and stock B are presented in SI Table S1.

2.4.3. Flow cytometry measurement

Stained samples were measured with a prototype of a CyFlow-Space (Partec, Görlitz, Germany), which is equipped with a 355-nm laser (50 mW, Genesis CX355-150-STM-OPSLaser-Diode System, Coherent, CA, USA). The laser was used to induce the forward scatter (FSC, bandpass filter 355 nm ± 5 nm) and side scatter (SSC, bandpass filter 355 nm ± 5 nm, trigger) signals and to excite the DAPI fluorescence (bandpass filter 455 nm C). Sheath buffer was 0.22 μm filtered Milli-Q water. UV beads [0.5 and 1.0 μm, both Fluoresbrite BB Carboxylate microspheres, (360/407), lot-no: 552744 and 659681, PolyScience, Niles, Illinois, USA] were used for instrument calibration on the logarithmic scale and were added to each sample for daily stability measurement. A biological standard [*Escherichia coli* K12, stationary phase of growth curve (16 h cultivation time in LB medium), fixed and stained as described before] was measured as a biological adjustment before and after sample measurement. DAPI-stained samples were measured cytometrically as logarithmically scaled 2D-dot plots according to DAPI fluorescence (DNA content) and FSC (cell size related) information. For every 2D-dot plot, 250,000 cells were measured within a master gate, which excluded instrumental noise and beads at a flow rate of 0.5 μL s^{-1} with the event speed below 1000 events s^{-1}. Detailed instrument operation can be found in Ref. [36].

2.4.4. Statistical data analysis

Cytometric data analysis and gate-template creation (SI Figure S4) was done using FlowJo V10 (FlowJo, LLC, Oregon, USA). In total, the gate-template included 20 gates, covering all subcommunities that appeared in 52 samples. All 52 cytometric 2D-plots can be accessed at the FlowRepository (https://flowrepository.org/experiments/2790) with Repository ID FR-FCM-Z2N6. The flowCyBar tool [31] (https://bioconductor.org/packages/release/bioc/html/flowCyBar.html) was used to visualize the cytometric community dynamics by using gate information of all samples.

2.5. Modelling using finite element method

2.5.1. Geometry and mesh

The finite element method (FEM) numerical solving program, COMSOL Multiphysics (Comsol Multiphysics GmbH, Göttingen, Germany), was used to sequentially solve Navier-Stokes (NS) and transport of diluted species (TDS) partial differential equations (PDEs) in order to estimate the velocity fields inside the reactor channels, and the convection, diffusion and reaction of the substrate acetate, respectively. The geometry of the setup is represented in SI Figure S5 for one electrochemical half-cell.

The base meshing of the geometry was done using the default "Fine" setting. This created a static polyhedral mesh with adequate size and number for the chosen physics NS. The mesh near the reaction surface (the bottom of the channels, where biofilms grow) was amended so that 16 planar boundary layers were constructed, with a stretching factor for the height dimension of each layer of 1.2. The mesh is composed of 910658 elements with an average element quality of 0.7404 and minimum element quality of 0.04372. A visual example of the mesh can be seen in SI Figure S5 B.

2.5.2. Modelling and boundary conditions

The NS flow equations were modeled assuming the liquid phase

as water ($\rho = 1000$ kg m^{-3}, $\mu = 0.001$ Pa s, T = 293.15 K). All the walls and internal surfaces (channel walls, electrode plates and membrane) were attributed to the boundary condition "no-slip", which assumes Newtonian behavior of the liquid and velocity of the liquid at these surfaces to be 0 m s^{-1}.

The liquid flow in the system was modeled with an inlet (the side "inlet" wall of channel 1), with a boundary condition of laminar inflow, set to a volumetric flow rate which is the maximum flow rate used experimentally for each reactor before the destructive sampling, and an outlet, the "outlet" side wall after channel 16, with the boundary condition of pressure-driven outflow, together with suppression of backflow. For easing the computational task, a first steady-state study was computed for solving NS flow alone for each flow rate. The resulting velocity fields inside the reactor (SI Figure S5 A is exemplary for reactor 2) were subsequently used to compute the steady-state solute convection, diffusion and reaction of acetate inside the anode chambers. Diffusivity for acetate was used as 1.089×10^{-9} m^2 s^{-1} accordingly [46] and an initial concentration of 10 mM acetate was assumed. Acetate consumption was simulated to only occur at the bottom surface of the channels, using Monod-type kinetics for *Geobacter sulfurreducens* [47] with $K_s = 0.03 \times 10^{-3}$ mol L^{-1}, and $\mu_{max} = 0.15$ h^{-1}. Here two types of simulations were made: a first approach, where total biomass (x) was considered as distributed homogeneously at the surface of every channel per reactor (SI Figure S5), and a second approach (SI Figure S6), where biomass per channel from the experimentally determined OD_{600} of each reactor was applied (SI Figure S7). To predict the here observed inhomogeneous biomass distribution a complex model beyond the applied Monod-type kinetics would have been needed that is not available.

3. Results & discussion

3.1. Physical-chemical benchmarking of the reactors

An initial modelling was performed in order to predict the growth and acetate consumption of *Geobacter* spp. inside the laminar flow BES. The expectations were that this microorganism dominates the electrode surface and consumes the acetate along channels of the reactor, leaving the further downstream channels limited in growth due to substrate depletion. The resulting ab-initio model confirmed these expectations, and the results are shown in SI Figure S5 B. From the SI Figure S5 B it is clear that under the assumed conditions (see above), the concentration of acetate inside the channels is gradually decreasing from the inlet channels to the outlet channels. Acetate is almost completely consumed leaving on average a residual 1 mM of acetate in the outlet. Further to the gradient in the flow direction, a concentration gradient is formed inside each channel from top to bottom. This is due to the consumption of acetate at the bottom of the reactor (that is at the anode) by a homogenous biofilm.

Quantification of the biomass inside each reactor (SI Figure S7) showed a heterogeneous biofilm distribution. The maximum biomass concentrations were found in channels 2 to 10 (depending on the moment in time when the reactors were stopped). This can be assigned to several reasons: i) the reactors were accidently exposed to the atmospheric oxygen near the inlets and outlets (due to an accidental failure of the gluing), inhibiting the growth of the EAM, ii) the nutrient-gradient dependent stratification led to the heterogeneous microbial distribution with the most robust and abundant microorganisms dominating the initial/middle channels, iii) the flow rate may selectively intercept certain microbial communities and lead to the heterogeneous microbial community distribution. Therefore, experimentally obtained OD_{600} data were used as an input parameter to model the steady-state acetate consumption. This allowed to obtain the acetate concentration profiles inside the reactors at the time of sampling (SI Figure S6). Furthermore, this biomass sampling shows that not all available anode area was covered with EAM biofilm, explaining the observed low current density (see next section).

3.2. Electrochemical performance

The three laminar flow BES were inoculated and operated identically, first in batch conditions for 7 days. In this time, the current gradually increased and reached a plateau (Fig. 1), indicating biofilm formation on the anode. Then the current decreased due to the depletion of the electron donor acetate. Before the current reached zero, the continuous mode was started. The three reactors were operated at increasing flow rates (HRT = 24 h from days 8–15, HRT = 17 h from days 16–20, all marked in light green). The current density reached steady-state between 41 and 57 μA cm^{-2} for all three reactors, with acetate removal efficiency averaging 94.4 ± 9.6%. Then reactor 1 was stopped and sampled for biofilm collection. Reactor 2 and 3 were further operated with higher flow rates (marked with middle green, HRT = 14 h). The sharp decrease in current density was due to a fortuitous error of the lack of trace element solution in the feed medium of the anode.

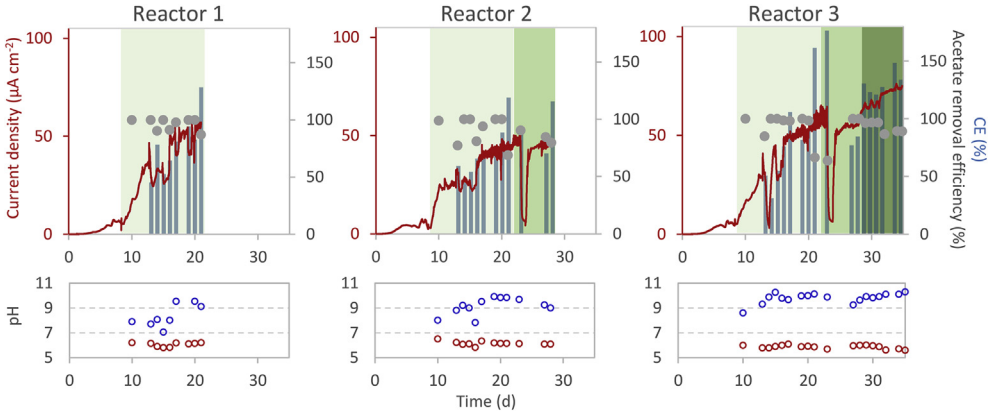

Fig. 1. Electrochemical performance of three reactors overtime, with green colors representing the decreasing HRT: HRT = 24 h from days 8-15 and HRT = 17 h from days 16-20 (light green), HRT = 14 h from days 21-28 (middle green), HRT = 12 h from days 29-35 (dark green). The current density (red curves, primary axis), acetate removal efficiency (grey dots, secondary axis) and the coulombic efficiency CE (blue bars, secondary axis) are shown in the first row. The pH is shown in the second row, red dots are the pH in the anode and blue dots are the pH in the cathode.

After replacing the medium with trace elements, the current recovered immediately and remained in the range of 46–56 μA cm^{-2}, with acetate removal efficiency up to 80–100%. Following, reactor 2 was stopped and sampled for biofilm collection, while reactor 3 was fed at the highest flow rate (marked with dark green, lowest HRT = 12 h). The current density kept increasing up to 75 μA cm^{-2}. Reactor 3 was stopped for biofilm collection on day 35. At this time, acetate was almost totally degraded (removal efficiency was 90%). Overall, with an acetate concentration of 10 mM, the current density ranged between 41 and 75 μA cm^{-2}, depending on the variable HRT. Higher current densities have been reported in the literature, with peak current density at graphite of up to 250 μA cm^{-2} [39] and 600 μA cm^{-2} [32], respectively, by using the same concentration of acetate in the medium. The main differences in current density values can be attributed to i) a ca. 27 times higher surface-area-to-volume ratio in our system (1770 cm^2 L^{-1}) than reported (64.5 cm^2 L^{-1}) [32], ii) the heterogeneous biofilm distribution in laminar flow systems, compared to the evenly biofilm-covered graphite rods. As mentioned, the maximum biomass was found in channels 2 to 10, and the other channels of available anode area were only covered with less biomass, and hence also fewer EAM. Generally, the CE was even most of the time exceeding 100%, indicating a possible diffusion inflow of hydrogen from the counter-electrode chamber [48]. The pH was stable all time at 5.6–6.5 in anode chamber and 7.7–10.3 in cathode chamber.

3.3. Analysis of the microbial community

Daily biofilm sampling of each channel was not possible due to construction limitations of the reactors. Intermittent sampling of the three reactors at different point of operation gave complementary understanding on the activity of microbial communities in response to time and variations in flow rate/nutrient gradient. The gained samples were cytometrically analyzed. The virtual cells per sample were clustered in diverse

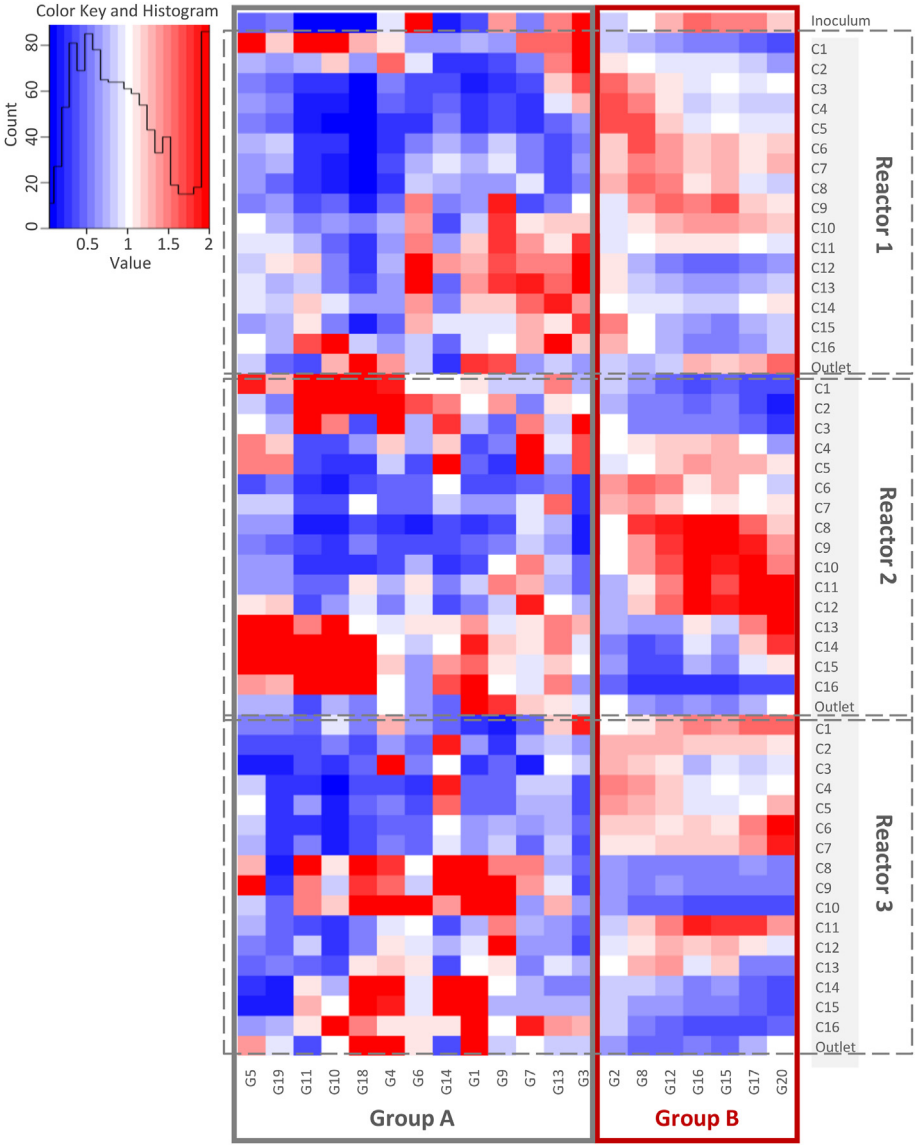

Fig. 2. Changes in the cytometric community structure of biofilms were visualized by using the flowCybar tool (https://bioconductor.org/packages/release/bioc/html/flowCyBar.html). The abundance of cells per each gate (x-axis) per channel (y-axis) is indicated by a color gradient, where dark blue corresponds to low cell abundance per gate, and red for high cell abundance per gate (see color key). Gates with cell numbers varying in similar directions were clustered, and can be visualized as Group A (G5 + G19 + G11 + G10 + G18 + G4 + G6 + G14 + G1 + G9 + G7 + G13 + G3), and Group B (G2 + G8 + G12 + G15 + G16 + G17 + G20). The relative cell abundance per gate is shown in SI Figure S8.

subcommunities according to their inherent cell information of light scattering and DNA content [49]. Whenever a new subcommunity became apparent, a gate was set (one subcommunity per gate (G)). The final gate-template with 20 gates (SI Figure S4) was created and applied to each sample in order to mirror the community structure changes and to extract individual cell abundances per gate [27]. Based on the extracted cell abundance per gate and sample, Fig. 2 gave a barcode of spatial-temporal changes in community structure. The cell abundance changes of each gate are indicated by a color gradient, where dark blue corresponds to low cell abundance per gate, and red to high cell abundance per gate. Gates that vary in similar directions were ordered according to the similarity as calculated in the heatmap, using values normalized by method "mean" (using the flowCybar tool in Fig. 2), and can be visualized as two groups: Group A (G5 + G19 + G11 + G10 + G18 + G4 + G6 + G14 + G1 + G9 + G7 + G13 + G3) and Group B (G2 + G8 + G12 + G15 + G16 + G17 + G20).

Overall, the flow cytometric analysis of the reactors, inoculated with a *Geobacter* spp. [32]. dominating culture as shown in the first row of barcode (Fig. 2), yielded a categorizing of two dynamic and distinct groups that formed inside the reactors during the time of BES operation. Six gates out of the 20 whose average value exceeds the threshold value are regarded as the dominant subcommunities (SI Figure S8), where two gates are from Group A [G4 (5.6 ± 4.4%) + G1 (9.7 ± 7.5%)], and four gates are from Group B [G2 (27.2 ± 7.7%) + G8 (13.0 ± 5.1%) + G12 (9.0 ± 3.7%) + G15 (5.9 ± 2.8%)]. The threshold is 4.7%, by determining the average cell abundance of all gates in all samples.

Most cells belonging to Group A were of relative smaller cell size and lower DNA content than cells of Group B (SI Figure S4). They also showed a lower cell abundance, averaging 34.3 ± 17.9% in all samples. They mainly grew up near the inlets and outlets (Fig. 3), where the reactors were accidently exposed to the atmospheric oxygen. In the middle channels, these cells in Group A were outcompeted by cells of Group B, which were predominant at those positions. Hence Group A cells might be more tolerant to the accidental exposure to oxygen, and they were active in growth when Group B declined.

Whole subcommunities of Group B strongly dominated almost all channels (Fig. 3, including inoculum and outlet samples) with high cell abundance on average of 65.7 ± 17.9%, regardless of whether the flow rate was low or high depending on the reactor operation. Thereof, Group B as a robust and vigorous group of subcommunities can survive in a wide range of acetate availabilities and flow rates, and assuredly contributed the most to the biomass value (SI Figure S7). It can be deduced that those gates in Group B contain very likely the "most" electroactive bacteria e.g. *Geobacter* spp. [35], which was dominant in the inoculum (Fig. 2 and SI Figure S9). They are known to degrade acetate up to 10 mM concentration [50], and are effective EAM. *Geobacter* spp. have also been reported to survive in low oxygen subsurface environments, and can be poised to rapidly take advantage of the development of anoxic conditions [51]. This could explain the lower cell abundances in the inlets and outlets, but the dominance in the middle channels.

When looking at the absolute biomass production in each reactor (SI Figure S7), in total more biomass was found at higher flow rates respectively at higher acetate availability. But the distribution of biomass was heterogeneous, most biomass was formed in the initial/middle channels (e.g. C2-10). This is accompanied by acetate stratification along the channels, with higher acetate availability at the beginning. The initial channel near the inlet had somewhat lower biomass formation, as it may have been inhibited by oxygen exposure. Much lower biomass was found near the outlet due to acetate depletion as well as accidental oxygen exposure.

Groups A and B were derived from the biofilms formed on the anode surface. In order to reveal the microorganisms represented by which group are the most relevant for current production, a correlation analysis was performed. Therefore, the total charge of a reactor (x-axis) was related to the relative biomass of the Group (y-axis).

In Table 1, the summed biomass of Group A and Group B in each reactor over time is shown. Both subsets presented a good correlation between biomass and total charge (Fig. 4), confirming that the biomass of the groups is intrinsically linked with electroactivity. Group B shows the highest slope of 1.4×10^{-3} OD_{600} C^{-1} ($R^2 = 0.95$), which indicates that the biomass formation of the microbial cells represented by this group is most effective. This correlation certainly has to be taken with care, as only three reactors are included and need to be set on a broader foundation. Further, Group B as the most abundant subcommunities dominated in and contributed to the high biomass in all channels.

4. Conclusion

Laminar flow electrochemical reactors for studying BES were established using 3D printing. The reactors were benchmarked using the archetype EAM *Geobacter* spp. and it was shown that:

Table 1
Biomass per reactor (indicated by OD_{600} as suspended in 1 mL of PBS) of Group A and B in each reactor, and the produced charge (Q_p) of each reactor.

	Reactor	Biomass	Q_p (C)
Group A	1 *(0–20 days)*	1.6	6585.2
	2 *(0–28 days)*	2.1	9736.8
	3 *(0–35 days)*	6.1	18354.1
Group B	1 *(0–20 days)*	5.8	6585.2
	2 *(0–28 days)*	6.4	9736.8
	3 *(0–35 days)*	21.0	18354.1

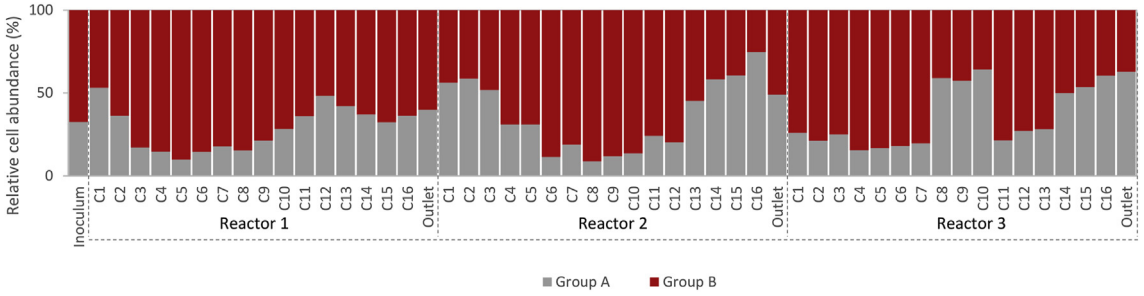

Fig. 3. Relative cell abundance distribution of Groups A and B in three reactors. The cell abundance of each group is obtained by summing the cell abundances of all subcommunities in each group. Group A and Group B are marked in grey and red, respectively. The cell abundance distribution in absolute biomass of each channel can be found in SI Figure S7.

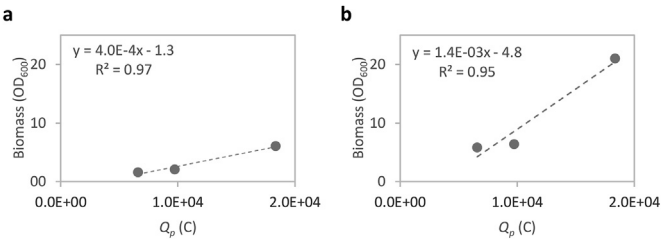

Fig. 4. (a). The correlation between the produced charge (Q_p) and biomass of Group A. (b). The correlation between the produced charge (Q_p) and biomass of Group B. Data are from Table 1.

i) Modeled substrate distribution and consumption using Monod-type kinetics indicates that the concentration gradients of the substrate acetate, found in flow direction as well as in the channel height could be linked to the experimental biomass heterogeneity effectively measured, with flow cytometry.
ii) The maximum current density of 75 μA cm^{-2} achieved at coulombic efficiencies of up to 100% can be assigned to the much higher anode surface area to volume ratio (here 1770 cm^2 L^{-1}), as well as the heterogeneous biomass coverage of the anode surface area.
iii) Stratification of electroactive microbial community structures and heterogeneous distributions of biomass were driven not only by substrate gradient but also by accidental oxygen exposure. The most robust and abundant electroactive organisms dominated all channels and contributed mostly to the current production, but biomass was formed mainly in the initial/middle channels.

The application of flow cytometry measurements in this study offered better insights into microbial community composition and structure changes inside the laminar flow reactor. The use of established bioinformatic tools to obtain and evaluate community data disclosed how microorganisms were stratified in the reactor channels. This information provides guidance for new designs of reactors where a more efficient operation is aimed. In follow-up studies different channel arrangements can be used, where only the initial/middle part of the reactor base needs to harbor current collector electrodes, while other parts (e.g. near the inlet and outlet) can be replaced with plastic to reduce the cost and limit the growth of electroactives to a "sweet-spot" zone where they will be more useful for the aimed process. In this case, also the membrane area and cathode chamber would be reduced. Therefore, areas of low biomass associated with current production would be minimized, and the resulting simple channels would be better for fermentative organisms. Additionally, understanding the stratification of microorganisms using a more complex substrate, for instance as we currently do for WW from the dairy industry [35], will offer possibilities to select and observe a wider range of electrochemically active and associated microorganisms for the degradation of complex organic matter, and allow engineering BES. Further, laminar flow reactors can be a promising option for microbial electrosynthesis as they will allow to carry out cascade reactions, coupling several synthesis steps in-line as already done for enzymatic electrosynthesis [52].

Declaration of competing interests

The authors declare that they have no known competing financial interests or personal relationships that could have appeared to influence the work reported in this paper.

Acknowledgements

This research is financed by the German Federal Ministry of Education and Research (BMBF) under the ElektroPapier project (Grant nr: 03XP0041G). The responsibility for the content lies with the authors. This work was supported by the Helmholtz-Association within the Research Programme Renewable Energies.

Appendix A. Supplementary data

Supplementary data to this article can be found online at https://doi.org/10.1016/j.ese.2020.100062.

References

[1] U. Schröder, F. Harnisch, L.T. Angenent, Microbial electrochemistry and technology: terminology and classification, Energy Environ. Sci. 8 (2015) 513–519, https://doi.org/10.1039/C4EE03359K.
[2] B.E. Logan, K. Rabaey, Conversion of wastes into bioelectricity and chemicals by using microbial electrochemical technologies, Science 337 (2012) 686–690, https://doi.org/10.1126/science.1217412.
[3] R.K. Brown, F. Harnisch, S. Wirth, H. Wahlandt, T. Dockhorn, N. Dichtl, et al., Evaluating the effects of scaling up on the performance of bioelectrochemical systems using a technical scale microbial electrolysis cell, Bioresour. Technol. 163 (2014) 206–213, https://doi.org/10.1016/j.biortech.2014.04.044.
[4] B.E. Logan, Exoelectrogenic bacteria that power microbial fuel cells, Nat. Rev. Microbiol. 7 (2009) 375–381, https://doi.org/10.1038/nrmicro2113.
[5] A. Kumar, L.H.-H. Hsu, P. Kavanagh, F. Barrière, P.N.L. Lens, L. Lapinsonnière, et al., The ins and outs of microorganism–electrode electron transfer reactions, Nat. Rev. Chem. 1 (2017), 0024, https://doi.org/10.1038/s41570-017-0024.
[6] S.G.A. Flimban, I.M.I. Ismail, T. Kim, S.-E. Oh, Overview of recent advancements in the microbial fuel cell from fundamentals to applications: design, major elements, and scalability, Energies 12 (2019) 3390, https://doi.org/10.3390/en12173390.
[7] S. Kerzenmacher, Engineering of microbial electrodes, in: F. Harnisch, D. Holtmann (Eds.), *Bioelectrosynthesis* Advances in Biochemical Engineering/Biotechnology, Springer International Publishing, Cham, 2017, pp. 135–180, https://doi.org/10.1007/10_2017_16.
[8] L. Koók, P. Bakonyi, F. Harnisch, J. Kretzschmar, K.-J. Chae, G. Zhen, et al., Biofouling of membranes in microbial electrochemical technologies: causes, characterization methods and mitigation strategies, Bioresour. Technol. 279 (2019) 327–338, https://doi.org/10.1016/j.biortech.2019.02.001.
[9] L.F.M. Rosa, S. Hunger, C. Gimkiewicz, A. Zehnsdorf, F. Harnisch, Paving the way for bioelectrotechnology: integrating electrochemistry into bioreactors, Eng. Life Sci. 17 (2017) 77–85, https://doi.org/10.1002/elsc.201600105.
[10] C.I. Torres, R. Krajmalnik-Brown, P. Parameswaran, A.K. Marcus, G. Wanger, Y.A. Gorby, et al., Selecting anode-respiring bacteria based on anode potential: phylogenetic, electrochemical, and microscopic characterization, Environ. Sci. Technol. 43 (2009) 9519–9524, https://doi.org/10.1021/es902165y.
[11] C. Koch, D. Popiel, F. Harnisch, Functional redundancy of microbial anodes fed by domestic wastewater, ChemElectroChem 1 (2014c) 1923–1931, https://doi.org/10.1002/celc.201402216.
[12] C. Koch, K.J. Huber, B. Bunk, J. Overmann, F. Harnisch, Trophic networks improve the performance of microbial anodes treating wastewater, npj Biofilms Microbiomes 5 (2019) 27, https://doi.org/10.1038/s41522-019-0100-y.
[13] K. Timmis, V. de Lorenzo, W. Verstraete, J.L. Ramos, A. Danchin, H. Brüssow, et al., The contribution of microbial biotechnology to economic growth and employment creation, Microb. Biotechnol. 10 (2017) 1137–1144, https://doi.org/10.1111/1751-7915.12845.
[14] C. Koch, B. Korth, F. Harnisch, Microbial ecology-based engineering of microbial electrochemical technologies, Microb. Biotechnol. 11 (2018) 22–38, https://doi.org/10.1111/1751-7915.12802.
[15] P.G. Dennis, B. Virdis, I. Vanwonterghem, A. Hassan, P. Hugenholtz, G.W. Tyson, et al., Anode potential influences the structure and function of anodic electrode and electrolyte-associated microbiomes, Sci. Rep. 6 (2016) 39114, https://doi.org/10.1038/srep39114.
[16] S. Ishii, S. Suzuki, T.M. Norden-Krichmar, T. Phan, G. Wanger, K.H. Nealson, et al., Microbial population and functional dynamics associated with surface potential and carbon metabolism, ISME J. 8 (2014) 963–978, https://doi.org/10.1038/ismej.2013.217.
[17] L. Rago, J.A. Baeza, A. Guisasola, Bioelectrochemical hydrogen production with cheese whey as sole substrate: bioelectrochemical hydrogen production with cheese whey, J. Chem. Technol. Biotechnol. 92 (2017) 173–179, https://doi.org/10.1002/jctb.4987.
[18] B. Virdis, F. Harnisch, D.J. Batstone, K. Rabaey, B.C. Donose, Non-invasive characterization of electrochemically active microbial biofilms using confocal Raman microscopy, Energy Environ. Sci. 5 (2012) 7017, https://doi.org/10.1039/c2ee03374g.
[19] S.D. Molenaar, T. Sleutels, J. Pereira, M. Iorio, C. Borsje, J.A. Zamudio, et al., In situ biofilm quantification in bioelectrochemical systems by using optical

coherence tomography, ChemSusChem 11 (2018) 2171–2178, https://doi.org/10.1002/cssc.201800589.
[20] A. Dewan, H. Beyenal, Z. Lewandowski, Scaling up microbial fuel cells, Environ. Sci. Technol. 42 (2008) 7643–7648, https://doi.org/10.1021/es800775d.
[21] C. Picioreanu, K.P. Katuri, I.M. Head, M.C.M. van Loosdrecht, K. Scott, Mathematical model for microbial fuel cells with anodic biofilms and anaerobic digestion, Water Sci. Technol. 57 (2008) 965–971, https://doi.org/10.2166/wst.2008.095.
[22] W. Liu, S. Cheng, Microbial fuel cells for energy production from wastewaters: the way toward practical application, J. Zhejiang Univ. - Sci. 15 (2014) 841–861, https://doi.org/10.1631/jzus.A1400277.
[23] J.M. Neumaier, A. Madani, T. Klein, T. Ziegler, Low-budget 3D-printed equipment for continuous flow reactions, Beilstein J. Org. Chem. 15 (2019) 558–566, https://doi.org/10.3762/bjoc.15.50.
[24] X. Zhu, M.D. Yates, M.C. Hatzell, H. Ananda Rao, P.E. Saikaly, B.E. Logan, Microbial community composition is unaffected by anode potential, Environ. Sci. Technol. 48 (2014) 1352–1358, https://doi.org/10.1021/es404690q.
[25] I. Schmidt, A. Pieper, H. Wichmann, B. Bunk, K. Huber, J. Overmann, et al., In situ autofluorescence spectroelectrochemistry for the study of microbial extracellular electron transfer, ChemElectroChem 4 (2017) 2515–2519, https://doi.org/10.1002/celc.201700675.
[26] C. Koch, A. Kuchenbuch, M. Marosvölgyi, K. Weisshart, F. Harnisch, Label-free four-dimensional visualization of anaerobically growing electroactive biofilms, Cytometry 97 (2020) 737–741, https://doi.org/10.1002/cyto.a.24169.
[27] C. Koch, F. Harnisch, U. Schröder, S. Müller, Cytometric fingerprints: evaluation of new tools for analyzing microbial community dynamics, Front. Microbiol. 5 (2014b), https://doi.org/10.3389/fmicb.2014.00273.
[28] C. Koch, H. Harms, S. Müller, Dynamics in the microbial cytome—single cell analytics in natural systems, Curr. Opin. Biotechnol. 27 (2014a) 134–141, https://doi.org/10.1016/j.copbio.2014.01.011.
[29] C. Koch, S. Müller, Personalized microbiome dynamics – cytometric fingerprints for routine diagnostics, Mol. Aspect. Med. 59 (2018) 123–134, https://doi.org/10.1016/j.mam.2017.06.005.
[30] Z. Liu, N. Cichocki, T. Hübschmann, C. Süring, I.D. Ofiţeru, W.T. Sloan, et al., Neutral mechanisms and niche differentiation in steady-state insular microbial communities revealed by single cell analysis: non-equilibria systems, Environ. Microbiol. 21 (2019) 164–181, https://doi.org/10.1111/1462-2920.14437.
[31] N. Cichocki, T. Hübschmann, F. Schattenberg, F.-M. Kerckhof, J. Overmann, S. Müller, Bacterial mock communities as standards for reproducible cytometric microbiome analysis, Nat. Protoc. 15 (2020) 2788–2812, https://doi.org/10.1038/s41596-020-0362-0.
[32] F. Harnisch, C. Koch, S.A. Patil, T. Hübschmann, S. Müller, U. Schröder, Revealing the electrochemically driven selection in natural community derived microbial biofilms using flow-cytometry, Energy Environ. Sci. 4 (2011) 1265, https://doi.org/10.1039/c0ee00605j.
[33] C. Koch, A. Kuchenbuch, J. Kretzschmar, H. Wedwitschka, J. Liebetrau, S. Müller, et al., Coupling electric energy and biogas production in anaerobic digesters – impacts on the microbiome, RSC Adv. 5 (2015) 31329–31340, https://doi.org/10.1039/C5RA03496E.
[34] N. Pous, C. Koch, A. Vilà-Rovira, M.D. Balaguer, J. Colprim, J. Mühlenberg, et al., Monitoring and engineering reactor microbiomes of denitrifying bioelectrochemical systems, RSC Adv. 5 (2015) 68326–68333, https://doi.org/10.1039/C5RA12113B.
[35] D.Y.A. Esquivel, Y. Guo, R.K. Brown, S. Müller, U. Schröder, F. Harnisch, Investigating community dynamics and performance during microbial electrochemical degradation of whey, ChemElectroChem 7 (2020) 989–997, https://doi.org/10.1002/celc.201902109.
[36] S. Günther, K. Faust, J. Schumann, H. Harms, J. Raes, S. Müller, Species-sorting and mass-transfer paradigms control managed natural metacommunities, Environ. Microbiol. 18 (2016) 4862–4877, https://doi.org/10.1111/1462-2920.13402.
[37] M.D. Besmer, D.G. Weissbrodt, B.E. Kratochvil, J.A. Sigrist, M.S. Weyland, F. Hammes, The feasibility of automated online flow cytometry for in-situ monitoring of microbial dynamics in aquatic ecosystems, Front. Microbiol. 5 (2014), https://doi.org/10.3389/fmicb.2014.00265.
[38] B. Buysschaert, L. Vermijs, A. Naka, N. Boon, B. De Gusseme, Online flow cytometric monitoring of microbial water quality in a full-scale water treatment plant, npj Clean Water 1 (2018) 16, https://doi.org/10.1038/s41545-018-0017-7.
[39] C. Gimkiewicz, F. Harnisch, Waste water derived electroactive microbial biofilms: growth, maintenance, and basic characterization, JoVE (2013), 50800, https://doi.org/10.3791/50800.
[40] J. Rodrigo Quejigo, L.F.M. Rosa, F. Harnisch, Electrochemical characterization of bed electrodes using voltammetry of single granules, Electrochem. Commun. 90 (2018) 78–82, https://doi.org/10.1016/j.elecom.2018.04.009.
[41] C. Koch, I. Fetzer, T. Schmidt, H. Harms, S. Müller, Monitoring functions in managed microbial systems by cytometric bar coding, Environ. Sci. Technol. (2013), https://doi.org/10.1021/es3041048, 130108105239000.
[42] L. Zacharoff, C.H. Chan, D.R. Bond, Reduction of low potential electron acceptors requires the CbcL inner membrane cytochrome of Geobacter sulfurreducens, Bioelectrochemistry 107 (2016) 7–13, https://doi.org/10.1016/j.bioelechem.2015.08.003.
[43] D.R. Bond, D.R. Lovley, Electricity production by Geobacter sulfurreducens attached to electrodes, Appl. Environ. Microbiol. 69 (2003) 1548–1555, https://doi.org/10.1128/AEM.69.3.1548-1555.2003.
[44] F. Harnisch, S. Freguia, A basic tutorial on cyclic voltammetry for the investigation of electroactive microbial biofilms, Chem. Asian J. 7 (2012) 466–475, https://doi.org/10.1002/asia.201100740.
[45] H. Liu, B.E. Logan, Electricity generation using an air-cathode single chamber microbial fuel cell in the presence and absence of a proton exchange membrane, Environ. Sci. Technol. 38 (2004) 4040–4046, https://doi.org/10.1021/es0499344.
[46] V. Petr, Ionic conductivity and diffusion at infinite dilution, in: Handbook Of Chemistry and Physics, CRC Press), Boca Raton, 1992, pp. 5-111–5–113. Available at: https://www.aqion.de/site/194.
[47] A. Esteve-Nunez, M. Rothermich, M. Sharma, D. Lovley, Growth of Geobacter sulfurreducens under nutrient-limiting conditions in continuous culture, Environ. Microbiol. 7 (2005) 641–648, https://doi.org/10.1111/j.1462-2920.2005.00731.x.
[48] B. Korth, A. KuchenbucH, F. Harnisch, Availability of hydrogen shapes the microbial abundance in biofilm anodes based on Geobacter enrichment, ChemElectroChem (2020), https://doi.org/10.1002/celc.202000731. In Press.
[49] Y. Guo, N. Cichocki, F. Schattenberg, R. Geffers, H. Harms, S. Müller, AgNPs change microbial community structures of wastewater, Front. Microbiol. 9 (2019) 3211, https://doi.org/10.3389/fmicb.2018.03211.
[50] S. Pinhal, D. Ropers, J. Geiselmann, H. de Jong, Acetate metabolism and the inhibition of bacterial growth by acetate, J. Bacteriol. 201 (2019), https://doi.org/10.1128/JB.00147-19 e00147-19.
[51] W.C. Lin, M.V. Coppi, D.R. Lovley, Geobacter sulfurreducens can grow with oxygen as a terminal electron acceptor, Appl. Environ. Microbiol. 70 (2004) 2525–2528, https://doi.org/10.1128/AEM.70.4.2525-2528.2004.
[52] S.D. Minteer, Oxidative bioelectrocatalysis: from natural metabolic pathways to synthetic metabolons and minimal enzyme cascades, Biochim. Biophys. Acta Bioenerg. 1857 (2016) 621–624, https://doi.org/10.1016/j.bbabio.2015.08.008.